

Full length article

Experimental findings and 2 dimensional two-temperature model in the multi-pulse ultrafast laser ablation on stainless steel considering the incubation factor



Luis Omeñaca, Santiago Miguel Olaizola, Ainara Rodríguez, Mikel Gomez-Aranzadi, Isabel Ayerdi, Enrique Castaño*

CEIT-Basque Research and Technology Alliance (BRTA), Manuel Lardizabal 15, 20018 Donostia/San Sebastián, Spain
Universidad de Navarra, Tecnun, Manuel Lardizabal 13, 20018 Donostia/San Sebastián, Spain

ARTICLE INFO

Keywords:

Ultrafast laser-metal interaction
Multi-pulse ablation
Incubation effect
Two-temperature model

ABSTRACT

The interaction between ultrashort laser pulses and metal targets is of great interest for machining and micro- or nano-processing applications. An experimental study was conducted on 316L stainless steel using ultrashort pulses with a duration of 280 fs and a wavelength of 1.032 μm. This study covered fluences ranging from 0.2 to 5 J/cm² and a number of pulses from 1 up to 200. The analysis of the experimental measurements has allowed us to better understand the process of laser-matter interaction and to obtain key parameters such as incubation effect or the change in the dominant ablation mechanism. By utilizing these parameters and thermophysical and optical dependencies for stainless steel, we have developed a 2D, two-temperature model (TTM), that allows precise and reliable determination of both ablation depth and diameter, which helps to reduce the number of necessary tests and avoid material waste.

1. Introduction

The development of ultrashort pulses with high peak power has led to active research into ultrafast laser-metal interaction. This is motivated by the need for micro and nanoscale machining and surface treatment. Ultrafast lasers, in contrast to continuous or longer pulses lasers, deposit energy more quickly, avoiding heat accumulation and achieving greater processing precision [1]. Ultrashort pulse ablation has proven its benefits over longer pulses in a wide range of fields, such as micro and nano machining [2], including the creation of laser-induced periodic surface structures (LIPSS) [3], surface structuring [4] and production of nanoparticles [5]. In order to enhance the efficacy and efficiency of laser processing, it is imperative to elucidate the interaction dynamics between the laser irradiation and metal. Consequently, a significant number of studies, encompassing both experimental and numerical approaches, have been conducted to this end. Nevertheless, the intricacy of this interaction and the multiplicity of physical mechanism involved in the ablation process present a significant challenge in determining the ablation parameters such as threshold fluence, or diameter and depth ablation, which remain a key objective in this research area.

It is generally accepted that the absorption of laser radiation in the material occurs in three stages. During the initial stage, laser energy is absorbed through the interaction of photons with the electrons of the metal. This is because heavy ions are unable to directly absorb the radiation, as they are unable to follow the rapid oscillation of the electromagnetic field. The remaining two stages are intimately connected, with one involving the diffusion and thermalization of the electrons within the lattice due to the thermal conductivity of the electrons themselves. The subsequent stage involves achieving the thermodynamic equilibrium with the ion lattice, which is accomplished through electron-phonon coupling. Following the energy distribution in the material, depending on the energy used, heating, melting or ablation of the metal will occur. Within the ablation, different mechanisms such as vaporization [6], fragmentation [6], spallation [7], and phase explosion [8] have been proposed. The efficiency and smoothness of the crater can be affected by this predominant ablation mechanism, which may interfere with subsequent pulses [9,10]. The mechanism may favour the ablation of the subsequent pulse due to the possible micro-roughness that appears, or alternatively, could reduce the efficiency of the next pulse due to the resolidification of ablated material. Furthermore, the

* Corresponding author at: CEIT-Basque Research and Technology Alliance (BRTA), Manuel Lardizabal 15, 20018 Donostia, San Sebastián, Spain.
E-mail address: ecastano@ceit.es (E. Castaño).

ablation depth of materials composed of different elements may vary due to the differing rates of removal of different elements. This can alter the material composition and consequently their properties regarding ablation [11]. In addition, in the case of multi-pulse ablation, other mechanisms emerge during the process that can affect ablation efficiency. The incubation effect is one such mechanism that reduces the fluence required to ablate the material as the number of pulses increases [12].

Due to the state of high non-equilibrium between the electron and ion lattices, a two-temperature model is necessary to describe the thermal evolution and, consequently, the ablation. Anisimov et al. [13] were the first to propose the two-temperature model (TTM), which uses two coupled equations to relate the electronic and lattice temperatures. Although hydrodynamic [14] or molecular dynamics [15] can simulate the process, the two-temperature model is the most widely used for studying the ablation of various materials due to its ability to produce a similar ablation profile, lower computational resource requirements and shorter processing time compared to these other models [16]. However, the majority of two-temperature models utilise either a single-pulse simulation [17,18], which can be in one or two dimensions, to obtain both depth and diameter, or one-dimensional multi-pulse simulations to obtain ablation depth, without taking into account the incubation effect, the possible compositional changes or the attenuation in ablation due to resolidified material [19,20]. This paper presents a two-dimensional two-temperature model that incorporates both the incubation effect within the model and the regime change between ablation through spallation and phase explosion.

2. Numerical modelling

2.1. Two-Temperature model

In the context of laser-metal interaction for ultrashort pulses, the absorption of radiation is carried out by electrons, while thermodynamic equilibrium is achieved through coupling between the electron and the lattice ions. The two-temperature model provides a comprehensive description of this process:

$$C_e \frac{\partial T_e}{\partial t} = \nabla(\kappa_e \nabla T_e) - G(T_e - T_i) + Q \quad (1)$$

$$C_i \frac{\partial T_i}{\partial t} = \nabla(\kappa_i \nabla T_i) + G(T_e - T_i) \quad (2)$$

The subscripts e and i refer to electronic or ionic subsystems, respectively. T denotes the temperature, C is the heat capacity, κ is the conductivity and G is the electron-ion coupling factor. The absorption of the laser pulse is described within the spatio-temporal source term Q , which can be divided into the following terms:

$$Q(r, z, t) = Q'(r, z) T(t) \quad (3)$$

The spatial contribution is calculated using the following formula:

$$Q' = \frac{1-R}{\delta} F \frac{w_0^2}{w^2} \exp\left(-\int_{z_s}^z \frac{1}{\delta} dz\right) \quad (4)$$

where R is the reflectance of the metal, δ is the effective penetration depth. For the simulations, we have taken δ to be 14 nm [21]. F is the laser fluence, w_0 is the radius of the laser beam at the focal plane. The laser fluence becomes position dependent with $w(z)$ as the laser drilling process is considered:

$$w(z) = w_0 \sqrt{1 + (z/z_R)^2} \quad (5)$$

Here z_R is the Rayleigh length, which depends on the wavelength and spot:

$$z_R = \pi w_0^2 / \lambda \quad (6)$$

Returning to Eq. (4), the lower limit of the integral z_s denotes the surface where the absorption occurs. This value is updated to match the new surface after each pulse. The temporal contribution of the laser pulse has the following form:

$$T(t) = \sqrt{\frac{4 \ln 2}{\pi t_p^2}} \exp\left(-2.77 \left(\frac{t-2t_p}{t_p}\right)^2\right) \quad (7)$$

with t_p denoting the full width at half maximum (FWHM) pulse duration, reaching its peak when $t = 2t_p$.

It is widely accepted that for laser-metal interaction ablation occurs when the ion temperature exceeds 0.9 the critical temperature T_c . In the specific case of the stainless steel, the critical temperature is $T_c = 10,360K$ [19].

2.2. Temperature dependencies

In order to obtain a more detailed and accurate model as was done in the case of aluminium [22], the dependencies of parameters appearing in Eqs. (1)-(2) with respect to the temperature have been taken into account.

2.2.1. Heat capacity

The electronic heat capacity C_e is fitted according to the theoretical results obtained from the study of density-functional theory (DFT) [23], utilising the fit performed by Metzner et al. [24]:

$$C_e = \left[2.68 \times 10^6 \exp^{8.94 \times 10^{-6} \frac{T_e}{K}} - 2.99 \times 10^6 \exp^{-3.79 \times 10^{-4} \frac{T_e}{K}} \right] \frac{J}{Km^3} \quad (8)$$

where K is the Kelvin unit used to ensure a correct dimensional analysis. The lattice heat capacity considering the phase transition of melting and evaporation [25] is given by:

$$C_i = C_{i0} + \Delta H_M \frac{1}{\Delta T \sqrt{2\pi}} e^{-\frac{1}{2} \left(\frac{T-T_M}{\Delta T}\right)^2} + \Delta H_V \frac{1}{\Delta T \sqrt{2\pi}} e^{-\frac{1}{2} \left(\frac{T-T_V}{\Delta T}\right)^2} \quad (9)$$

where $C_{i0} = 450 J/KgK$, ΔT determines the width of the zone of phase change and is set to 50 K. T_M , and T_V are the melting and vaporization temperatures for stainless steel respectively, while ΔH_M and ΔH_V are the latent heat of fusion and of vaporization, respectively.

2.2.2. Thermal conductivity

The mechanism for heat conduction in metals is diffusion of free electrons, κ_e is usually the dominant contribution. Nevertheless, the ion thermal conductivity is not neglected in this TTM and is taken as 1% ($\kappa_i \approx 0.01\kappa_e$) of the overall thermal conductivity [17,26]. The electronic thermal conductivity is derived from the experimental data obtained by Kim et al. [27] for 316L stainless steel, and the data for temperatures above the melting point have been extrapolated:

$$\kappa_e(T_i < T_M) = \left(9.21 + 0.0157 \frac{T_i}{K} \right) \frac{W}{Km} \quad (10)$$

$$\kappa_e(T_i \geq T_M) = \left(12.41 + 3.279 \frac{T_i/K}{1000} \right) \frac{W}{Km}$$

2.2.3. Electron-ion coupling

For the coupling between the electron and ion lattices, the DFT study/Metzner fit [23,24] is used again:

$$G = \left[2.84 \times 10^{18} \exp\left(-\frac{(T_e - 3077)}{1.17 \times 10^4}\right)^2 + 2.99 \times 10^{18} \exp\left(-\frac{(T_e - 2.99 \times 10^4)}{8.15 \times 10^4}\right)^2 \right] \frac{W}{Km^3} \quad (11)$$

2.2.4. Reflectivity

The optical dependencies of the major elements present in the steel 316L were investigated through the DFT study/ Metzner fit [23,24]. The elements were weighted to calculate the reflectance as a function of the electronic temperature:

$$R = 0.11 \exp^{-1.3 \times 10^{-4} T_e / K} + 0.59 \quad (12)$$

2.3. Geometric mesh

To resolve Eqs. (1) and (2), we employed the finite-difference time-domain (FDTD) method with a forward time centered space (FTCS) scheme, utilising our in-house Python code. The finite elements were optimised to reduce processing time while satisfying stability and consistency criteria [28]. Due to the axial symmetry of the process, the simulation can be simplified to a two-dimensional mesh, as illustrated in Fig. 1 with $dr = 0.1 \mu m$ and $dz = 2.5 nm$. The stainless steel temperature is set at the ambient temperature $T_0 = 300K$. The laser source maximum for the first pulse is located at $r = z = 0$. A zero-flux condition has been imposed on the right and bottom boundaries, as well as on the top boundary due to negligible radiation losses [17].

Given that a pulse frequency of 5 kHz is employed, it is expected that the temperature will return to ambient conditions before the next pulse [29]. Consequently, each pulse is simulated divided in steps of 3.5 fs from $t = 0$ to $t = 15 ps$, where the crucial interaction takes place. Following each pulse, the value of z_s is updated to reflect the new non-ablated surface, where the laser absorption begins. The temperature of the unablated material is then reset to T_0 .

$$Te(r, z, t_0^N) = T_i(r, z, t_0^N) = T_0 \quad (13)$$

$$\frac{\partial T_e}{\partial n} \Big|_{\Omega} = \frac{\partial T_i}{\partial n} \Big|_{\Omega} \quad (14)$$

where t_0^N is the initial time of pulse N and Ω represents the top, right and bottom surfaces of the stainless steel.

For a low number of pulses, this mesh is sufficient. However, as the number of pulses increases, it becomes necessary to expand the mesh to

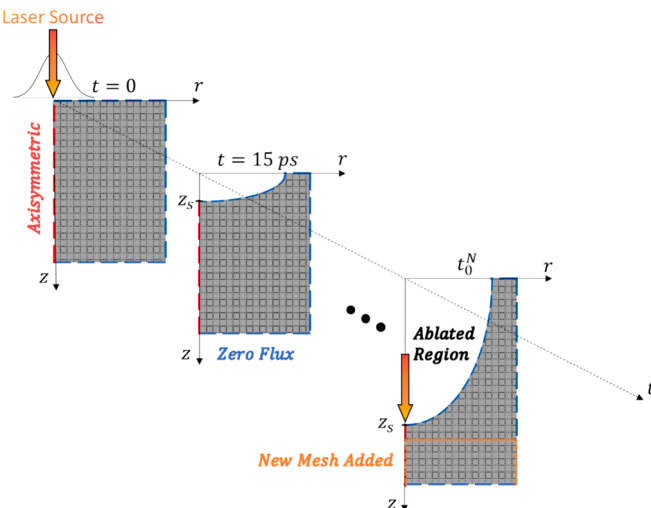


Fig. 1. Schematic diagram of simulated stainless steel mesh when irradiation starts ($t = 0$), first pulse finish ($t = 15 ps$) and pulse N starts (t_0^N). Incubation effect.

simulate the entire ablation process. In the code, if the unablated material is less than 25% of the mesh in the Z direction, the depth is increased by $0.5 \mu m$. This method of generating the mesh results in a significant reduction in computation compared to creating a large mesh from the outset.

2.4. Incubation effect

Experimental results have demonstrated that the incubation effect occurs during multi-pulse interaction in metals [11,29–31]. While the physical mechanisms behind this phenomenon remain unclear, the formation of micro- and sub-microstructures is believed to be responsible for the observed effect, which impacts the material's reflectivity [11]. The incubation effect has been observed to result in a reduction in the fluence required for material ablation to decrease as the number of pulses increases. This phenomenon can be modelled as follows [32]:

$$F_{Th}(N) = F_{Th}(1)N^{S-1} \quad (15)$$

where $F_{Th}(N)$ is the threshold fluence for pulse number N , $F_{Th}(1)$ is the threshold fluence for mono-pulse, and S is the incubation factor. Consequently, the incubation factor can be determined by knowing the threshold fluence values at different numbers of pulses and performing a curve fitting. An experimental study detailed in Section 4.1 was conducted to determine the value of the incubation factor. To include the incubation effect in our two-temperature model, we used the correlation between the threshold fluence and the optical properties [30]:

$$F_{Th}(N) = \frac{\rho \Omega_{Vap}}{\alpha A} \quad (16)$$

where ρ is the density of stainless steel, Ω_{Vap} is the specific heat of evaporation, α is the absorption coefficient and A is the absorbance, defined as $A = 1 - R$. Several studies have demonstrated a correlation between the number of pulses in the right term of Eq. (16) and the reflectance [11,30]. Therefore, we can introduce the incubation effect into our model by combining Eqs. (4), (15) and (16):

$$Q'(N) = \frac{AN^{1-S}}{\delta} F \frac{w_o^2}{w^2} \exp\left(-\int_{z_s}^z \frac{1}{\delta} dz\right) \quad (17)$$

This new absorption will be used when the lattice temperature at a mesh point is equal to or exceeds the vaporization temperature. It is hypothesised that this is the point at which micro- and sub-micro structures are created, which in turn affects the reflectivity of the material. In order to incorporate the incubation effect into the simulation, each point in the mesh will be assigned a value for N , which will be updated in accordance with whether the lattice temperature value from the previous pulse has exceeded the vaporization value in the corresponding mesh point.

2.5. Ablation mechanisms

In the case of certain metals, experimental measures of the depth as a function of the fluence have demonstrated the existence of two distinct ablation regimes [9,10,33–35]. These regimes appear to be distinguished by a change in the primary ablation mechanism [10,36,37]. At lower fluence values, the dominant mechanism is spallation [7] of a single or multiple layer. In contrast, for higher fluence values, explosive disintegration of a superheated surface layer (phase explosion) [8] is the predominant mechanism. In certain metals, a higher ablation rate per pulse can be favoured by utilizing the phase explosion mechanism, due to the increase in depth per pulse being significantly greater than the possible losses in the next pulse due to redeposition or changes in reflectivity [33,38,39]. However, for steel, due to its low penetration depth, the significant change in crater morphology depending on the ablation regime, the use of a high fluence regime does not appear to be a viable option for increasing ablation efficiency, as evidenced by the

findings of [10,40]. In addition to this effect, it is also important to consider how laser interaction can modify the composition of alloys. As some of these elements are more easily ablated, the ablation rate will decrease as the accumulated fluence increases. This resembles the ablation rate of the most difficult element to ablate [11]. In order to incorporate the ablation regime and compositional changes into the model, a parameter in laser absorption, denoted as absorption attenuator (Δ), has been introduced:

$$Q''(N, F) = \Delta(N, F)Q(N) \quad (18)$$

This factor is dependent on both the fluence and the number of pulses. As the fluence value increases beyond a certain threshold, the ablation mechanism changes, leading to more material being ablated and a more drastic reconstitution. Furthermore, the alteration of the reflectivity of the material, resulting from the modification of the initial polished surface, microroughness generated by ablation and the incubation effect can favour the change in ablation mechanism to a lower fluence as the number of pulses is increased. The dependency on these parameters has been experimentally obtained in Section 4.2.

3. Experimental work

In order to obtain the incubation value, the attenuator factor and to verify and validate the model, it is necessary to perform laser shots on stainless steel under several conditions of fluence and pulse numbers. The different conditions that have been used are shown in Table 1. Stainless steel 316L was used and previously polished with *SiC* papers, making the surface roughness $S_a < 50 \text{ nm}$. This was done in order to reduce the potential influence of roughness on the laser ablation, while also allowing for measurements to be made at low fluences a low number of pulses.

To attain the stipulated conditions, a diode-pumped ultrafast fibre laser system (*Amplitude Satsuma HP*) with a wavelength of $\lambda = 1032 \text{ nm}$, a spot size of $w_0 = 10 \mu\text{m}$, and pulse duration of $t_p = 280 \text{ fs}$ is used. This laser has a maximum average power of $P = 10 \text{ W}$ at a repetition rate of 500 kHz . The micromachining setup (*LASEA LS-Lab*) employs a variety of modules to adjust and control the laser power, spot size, frequency and processing time to achieve the conditions outlined in Table 1 at a frequency of 5 kHz . To characterise the ablation craters obtained and to measure both their depth and diameter, an optical profilometer was employed (*Sensofar S Neox*), utilising the interference technique with a $50\times$ objective (Nikon DI $50\times$). Prior to processing, the sample was cleaned in an ultrasonic bath with acetone, followed by ethanol before and after processing. Each of these steps was carried out for two minutes. Despite the implementation of these treatments, the material continued to exhibit irregularities and defects. In order to obtain robust measurements of both depth and diameter, 25 processes were performed for each condition, as illustrated in Fig. 2. Subsequently, measurements of diameters and depths were taken for the 10 best processes obtained for each condition.

4. Results and discussion

4.1. Incubation effect

Various incubation models have been proposed in the literature [41], however, in order to incorporate it into our TTM, we adopt the most extended, presented in Eq. (15). In order to determine the incubation factor S , it is necessary to determine the threshold fluence values for

Table 1
Laser parameters.

Parameter	Laser fluence (J/cm^2)	Pulse number (-)
Values	0.22, 0.45, 0.67, 0.89, 1.5, 2.5, 3.5, 4.5, 5.5.	1, 5, 10, 25, 50, 75, 100, 200

different number of pulses. The most widely accepted method for obtaining this value is to measure the diameters with Liu's method [42]:

$$D^2(N) = 2w_0^2 \ln\left(\frac{F}{F_{Th}(N)}\right) \quad (19)$$

The values of $F_{Th}(N)$ can be obtained by measuring the diameters and knowing both the number of pulses and the fluences employed. Fig. 3 shows the threshold fluence values derived from the fit with Eq. (19) plotted against the number of pulses. It is evident that the threshold fluence decreases as the number of pulses increases, eventually stabilising.

By fitting these values to Eq. (15), we obtain a value for the incubation factor, $S = 0.85 \pm 0.01$. The obtained value falls within the generally accepted range for metals, where the incubation factor ranges between $0.8 - 0.9$ [35,43]. The obtained value is consistent with literature values, Orlandini et al. [44] retrieved a value of $S = 0.85 \pm 0.05$, Zhou et al. [45] recovered $S = 0.85 \pm 0.01$ and Metzner et al. [24] obtain a value for stainless steel of $S = 0.81 \pm 0.04$.

4.2. Absorption attenuation

The objective of this section is to investigate the influence of pulse number and fluence on the ablation regime and variation in composition, and consequently, the ablation depth. To investigate how the ablation depth is affected, we can examine the ablation rate, which is the depth divided by the number of pulses. Fig. 4 shows the ablation rate for the experimental measurements. At this juncture, it is possible to distinguish between two distinct zones based on fluence. In the first zone, which is characterized by a prevalence of incubation, the ablation rate increases in tandem with the number of pulses. Conversely, in the second zone, which is characterised by a prevalence of attenuation, the ablation rate is higher with fewer pulses. To gain a more comprehensive understanding of the relationship between the number of pulses and fluence, we have defined the absorption attenuator as the relative variation between the ablation rate value for pulse N and single pulse, at a given fluence F :

$$\Delta(F, N) = \frac{\text{Ab.Rate}(F, N)}{\text{Ab.Rate}(F, 1)} \quad (20)$$

By calculating the Δ values for our experimental measurements, we can affirm that incubation dominates for fluence values $< 1.5 \text{ J}/\text{cm}^2$. However, for fluences above this threshold, the change in the ablation mechanism, which leads to an increased redeposition of resolidified material and changes in the composition, becomes more pronounced, increasing linearly with fluence and growing with the number of pulses, until reaching a value of 10 pulses, where the effect seems to saturate. In light of the aforementioned considerations, we have defined a function $\Delta(F, N)$, which can be introduced into our model using Eq. (18):

$$\Delta(F, N) = \begin{cases} 1, F \leq 1.5 \text{ J}/\text{cm}^2, \\ \Delta(N), F > 1.5 \text{ J}/\text{cm}^2 \end{cases} \quad (21)$$

$$\Delta(N) = \begin{cases} 1 + (g(F) - 1) \left(\frac{N-1}{10-1} \right), N \leq 10, \\ g(F), N > 10 \end{cases} \quad (22)$$

$$g(F) = 1.16 - 0.091F \quad (23)$$

Here, Eq. (23) uses the fit represented in the small inset of Fig. 4. In $\Delta(F, N)$ function, the possible effects that cause our ablation depth to be lower than expected have already been accounted for, resulting in a linear trend with these fluences, as increasing the fluence leads to increased redeposition of material. However, this trend is only observed when the number of pulses is equal to or greater than 10, when the number of pulses is less, Eq. (22) applies a correction factor making the effect less noticeable as the number of pulses decreases. We propose that

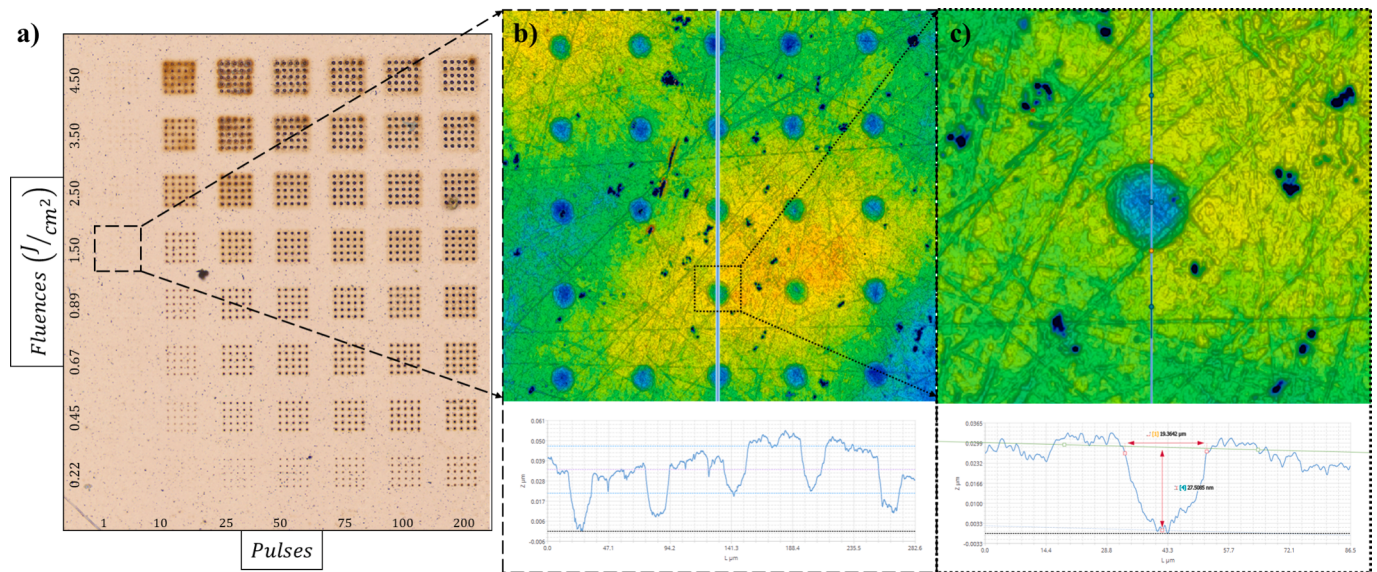


Fig. 2. Measures taken with Sensofar. (a) Image depicting laser processes performed on steel. (b) Interferometric measurement with x50 objective for 1 pulse and fluence of $1.5 J/cm^2$. (c) Region of interest to obtain the depth and diameter ablation of a crater.

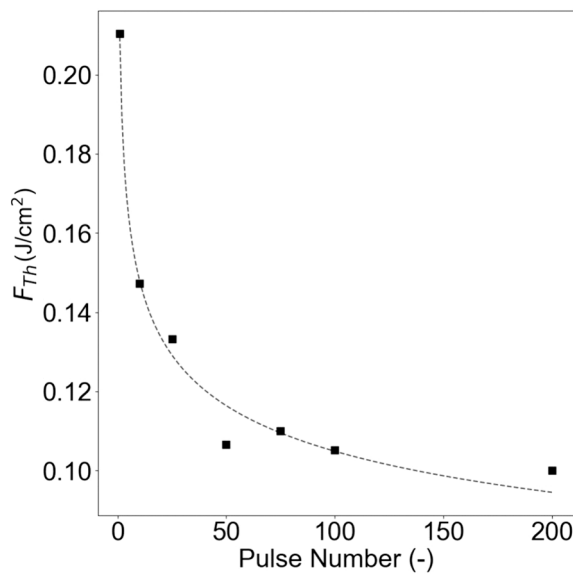


Fig. 3. Squares represent the experimental values and line the corresponding fit.

this correction is primarily attributable to the observation that as the number of pulses increases, the transition from spallation to phase explosion as the dominant ablation mechanism occurs at progressively lower fluences, stabilising around a fluence of $1.5 J/cm^2$ at 10 pulses. In addition, we posit that the change in composition as the fluence is increased will result in greater variation of this attenuation [11]. The main components present in stainless steel 316L are iron (70%), chromium (17%) and nickel (10%). On one hand, both iron and chromium exhibit similar optical properties as well as a comparable threshold fluence. For iron we have the following values: $\delta^{Fe} = 21 nm$ and $F_{Th}^{Fe}(1) = 0.23 J/cm^2$ [46]. For chromium, the values are: $\delta^{Cr} = 23 nm$ and $F_{Th}^{Cr}(1) = 0.19 J/cm^2$ [47]. However, nickel is more challenging to ablate, as it exhibits values: $\delta^{Ni} = 14 nm$ [48] and $F_{Th}^{Ni}(1) = 0.40 J/cm^2$ [49]. From these values we can see that the first elements to be removed are both chromium and iron, and as we increase the number of pulses it

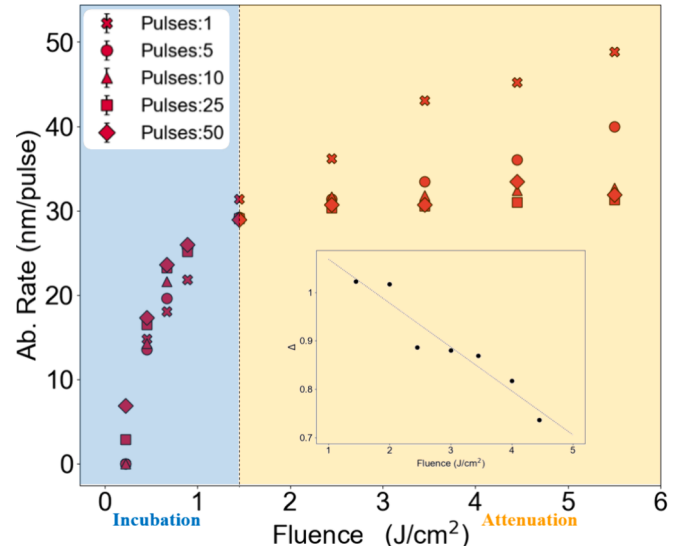


Fig. 4. Ablation rate vs fluences for different number of pulses. In the blue region, incubation prevails, in the orange, attenuation dominates. In the small inset, Δ corresponding to 10 pulses is represented.

becomes more difficult. Finally, using Eq. (21), we are able to differentiate the zone where incubation dominates, and the ablation rate increases with the number of pulses, from the zone where the effects that reduce this ablation rate prevail. One might expect this value to vary with the number of pulses; however, from the experimental results obtained, it appears to be very stable, at least from 10 pulses onwards. A more detailed study should be conducted for a number of pulses between 1 and 10, including an investigation of composition.

4.3. Numerical validation

After obtaining the incubation factor value and ablation attenuator, simulations were conducted using our model. The fluences used in these simulations were the same as those proposed experimentally, and some values in the range between 0.2 to $4.5 J/cm^2$. The number of pulses ranges from 0 to 100. The results and comparisons have been divided

into single- and multi-pulse.

4.3.1. Mono-pulse

For the single-pulse case, a logarithmic trend emerges for depth with fluence as can be seen in Fig. 5. This dependence has been parameterized based on material and radiation parameters as follows [50]:

$$\text{Depth} = \delta \ln(F/F_{Th}) \quad (24)$$

Fitting the experimental values obtained to Eq. (24), we retrieved a value for penetration depth of $\delta_{exp} = 13.8 \pm 0.7 \text{ nm}$, while for the simulation values we obtain $\delta_{sim} = 14.0 \text{ nm}$, we can see that both values are in good agreement.

Furthermore, when compared with values retrieved from other authors, Lickschat et al. [21] determine an experimental value of $\delta = 11 \text{ nm}$ at $t_p = 0.2 \text{ ps}$ and $\lambda = 1030 \text{ nm}$. Winter et al. [51] obtain a value of $\delta = 15 \text{ nm}$ for AISI304 with a $t_p = 525 \text{ fs}$ and $\lambda = 1056 \text{ nm}$. The threshold fluence value for the single-pulse case can also be obtained from (24), in the experimental case, a value of $F_{Th}^{exp}(1) = 0.18 \pm 0.03 \text{ J/cm}^2$, while for simulation $F_{Th}^{sim}(1) = 0.20 \text{ J/cm}^2$. These obtained values are slightly low, as from the experimental study, it has been observed that there is no ablation for the fluence of 0.22 J/cm^2 . However, the method for obtaining the threshold fluence through depth is not as precise as the Liu's method [51], therefore we will use the diameter value for comparison with the literature. We use Eq. (19), with $N = 1$. Performing the curve fitting using our spot size of $10 \mu\text{m}$, and the values showed in Fig. 5(b) we obtain a threshold fluence value of $F_{Th}^{exp}(1) = 0.25 \pm 0.02 \text{ J/cm}^2$, and fitting the simulated results retrieved a value of $F_{Th}^{sim}(1) = 0.27 \text{ J/cm}^2$. These values are in better agreement with the experimentally analysed results. Additionally, comparing with other authors, we can see that the value is also very similar, Lickschat [21] obtain a value $F_{Th}(1) = 0.26 \text{ J/cm}^2$, Orlandini et al. [44] calculate a value $F_{Th}(1) = 0.29 \pm 0.09 \text{ J/cm}^2$ and Zhou et al. [45] get $F_{Th}(1) = 0.29 \pm 0.10 \text{ J/cm}^2$.

4.3.2. Multi-pulse

In the validation on multi-pulse ablation, both experimental and corresponding simulated crater depth results are presented in Fig. 6. We can observe that the trends of the experimental and simulated results are in agreement. For low fluence values, the simulations underestimate the experimental findings. This discrepancy may be attributed to the approximate manner in which incubation is introduced in our model. However, for higher fluences, above 1.5 J/cm^2 , simulated values begin to overestimate the experimental results. The deviations in this zone may arise from the different assumptions we have made to replicate the different effects within the model.

In Fig. 6 we have the comparison of experimental and simulated

results for diameter. To the best of the author's knowledge, this is the first two-temperature model capable of incorporating incubation to obtain ablation depths for fluence below the single-pulse threshold fluence.

This is observed in the case of the lowest fluence of 0.22 J/cm^2 , in the mono-pulse study, no ablation occurs, however, thanks to the incorporation of the incubation effect in the model, ablation appears as the number of pulses increases for this fluence. In addition, we can see that the values for low pulse numbers for both simulation and experimental data are in good agreement. However, as we increase the number of pulses, the increase in diameter is much more noticeable in the experimental values. This could be due to how we introduce attenuator Δ into the model, as it affects the total absorption of the material. This effect should be much more localized in the central regions of the ablation because, due to the Gaussian shape of the beam, besides phase explosion in the centre, spallation may still occur at the edges of the ablation favouring incubation [52].

5. Conclusions

In this paper, we have experimentally investigated ultrafast laser ablation both in single-pulse and multi-pulse for stainless steel. Subsequently, we have improved the two-temperature model taking into account the various effects observed in the experimental study, and we have validated the results by comparing both. From the experimental values, we have been able to obtain key parameters for ablation, such as the experimental penetration depth δ^{exp} and pulse number dependent threshold fluence $F_{Th}(N)$, although this value can be calculated using both the diameter and the depth of ablation, it is more accurate to obtain it through the diameter because depth measurements are affected by additional factors that make it more challenging to extract the real value. $F_{Th}(N)$ decreases with the number of pulses until a certain number where this value seems to stabilize. With these threshold fluence values, we can obtain the factor of incubation for stainless steel, we have retrieved a value of $S = 0.85$ which is consistent with data presented by other authors for this material. This incubation effect enhances the ablation in both diameter and depth. In addition to this improvement effect on ablation, we can observe the effect of ablation mechanism and variation in composition, which minimises the ablation rate. These effects start to become noticeable from a fluence of 1.5 J/cm^2 and increase with it. Moreover, concerning the number of pulses, it also appears that they increase as the number of pulses rises until stabilizing for 10 pulses. These degradation effects on ablation become particularly significant at higher fluences within our range, causing the ablation rate to decrease by up to 30% of the expected value. Thanks to this experimental study, we have been able to create an improved two-temperature model that considers these distinct effects. In particular, thanks to this model,

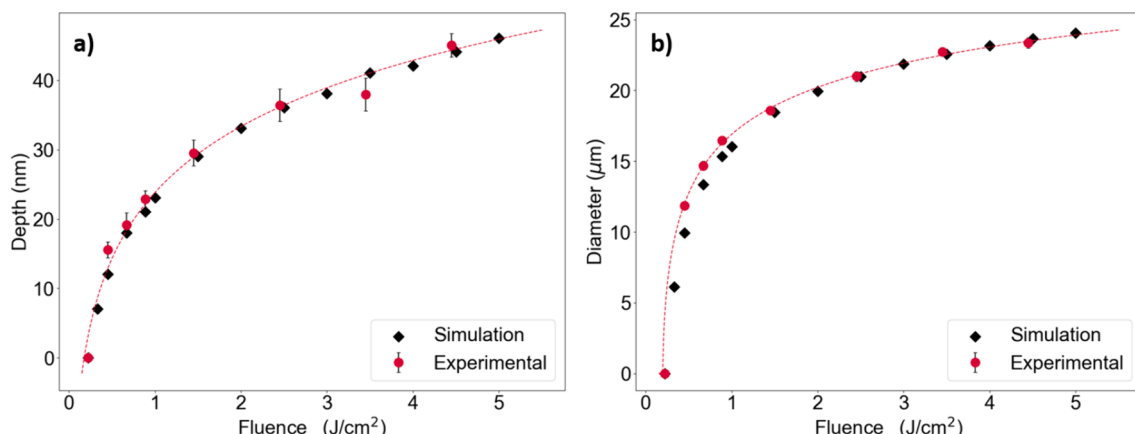


Fig. 5. Experimental (red) and simulation (black) values for mono-pulse ablation. (a) Depth. (b) Diameter.

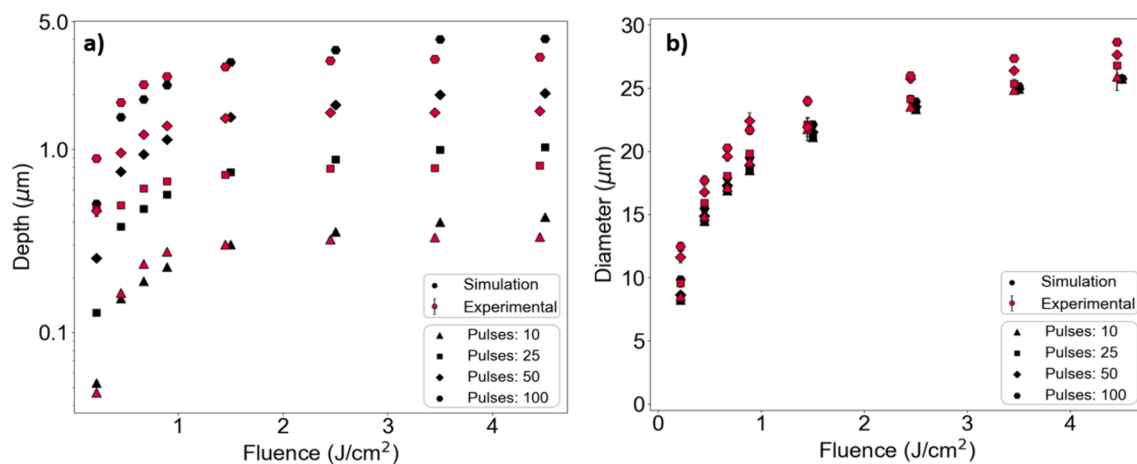


Fig. 6. Experimental (red) and simulation (black) values for multi-pulse ablation at different pulses. (a) Depth. (b) Diameter.

ablation for fluences below the threshold fluence for a single pulse is achieved as we increase the number of pulses, and the value of $F_{Th}(N)$ is lower than the used fluence. Finally, we obtained highly consistent data for the mono-pulse study, both in depth and diameter, yielding very similar threshold fluence values, as well as consistent trends for the multi-pulse case.

Declaration of generative AI and AI-assisted technologies in the writing process

Statement: During the preparation of this work the authors used ChatGPT in order to improve readability and language. After using this tool, the authors reviewed and edited the content as needed and take full responsibility for the content of the publication.

CRediT authorship contribution statement

Luis Omeñaca: Conceptualization, Methodology, Software, Validation, Formal analysis, Investigation, Resources, Data curation, Writing – original draft, Visualization. **Santiago Miguel Olaizola:** Writing – review & editing, Supervision, Resources, Project administration. **Ainara Rodríguez:** Writing – review & editing, Validation, Supervision. **Mikel Gómez-Aranzadi:** Writing – review & editing, Validation, Supervision, Resources, Investigation. **Isabel Ayerdi:** Writing – review & editing, Validation, Supervision, Resources. **Enrique Castaño:** Writing – review & editing, Validation, Supervision, Methodology, Formal analysis, Conceptualization.

Declaration of competing interest

The authors declare that they have no known competing financial interests or personal relationships that could have appeared to influence the work reported in this paper.

Data availability

Data will be made available on request.

Acknowledgments

This work has been sponsored by Horizon Europe Digital, Industry and Space Programme under Grant No. 101091623.

References

- [1] B.N. Chichkov, C. Momma, S. Nolte, F. Von Alvensleben, A. Tünnermann, Femtosecond, picosecond and nanosecond laser ablation of solids, *Appl. Phys. A* 63 (1996) 109–115.
- [2] L. Mizzi, E. Salvati, A. Spaggiari, J.C. Tan, A.M. Korsunsky, Highly stretchable two-dimensional auxetic metamaterial sheets fabricated via direct-laser cutting, *Int. J. Mech. Sci.* 167 (2020) 105242, <https://doi.org/10.1016/j.ijmecsci.2019.105242>.
- [3] A. San-Blas, et al., Femtosecond laser fabrication of LIPSS-based waveplates on metallic surfaces, *Appl. Surf. Sci.* 520 (2020) 146328.
- [4] S. Milles, J. Dahms, B. Voisiat, S. Indrišiūnas, G. Raciukaitis, A.F. Lasagni, Wetting properties of aluminium surface structures fabricated using direct laser interference patterning with picosecond and femtosecond pulses, *J. Laser Micro Nanoeng.* 16 (1) (2021) 74–79.
- [5] T. Donnelly, G. O'Connell, J.G. Lunney, Metal nanoparticle film deposition by femtosecond laser ablation at atmospheric pressure, *Nanomaterials* 10 (11) (2020) 2118.
- [6] L.J. Lewis, D. Perez, Laser ablation with short and ultrashort laser pulses: Basic mechanisms from molecular-dynamics simulations, *Appl. Surf. Sci.* 255 (10) (2009) 5101–5106.
- [7] J. Cheng, et al., A review of ultrafast laser materials micromachining, *Opt. Laser Technol.* 46 (2013) 88–102.
- [8] S. Bruneau, J. Hermann, G. Dumitru, M. Sentis, E. Axente, Ultra-fast laser ablation applied to deep-drilling of metals, *Appl. Surf. Sci.* 248 (1–4) (2005) 299–303.
- [9] H.D. Nguyen, et al., Super-efficient drilling of metals with ultrafast non diffractive laser beams, *Sci. Rep.* 12 (1) (2022) 2074.
- [10] P. Lickschat, A. Engel, D. Metzner, A. Horn, S. Weißmantel, Experimental study on the ablation of stainless steel using multiple ultra-short laser pulses with tunable time delays, *Appl. Phys. A* 129 (10) (2023) 674.
- [11] C. McDaniel, A. Flanagan, G.M. O' Connor, Evidence for increased incubation parameter in multi-pulse ablation of a Pt:SS alloy using a femtosecond laser at high repetition rates, *Appl. Surf. Sci.* 295 (2014) 1–7, <https://doi.org/10.1016/j.apsusc.2013.12.034>.
- [12] J. Bonse, P. Rudolph, J. Krüger, S. Baudach, W. Kautek, Femtosecond pulse laser processing of TiN on silicon, *Appl. Surf. Sci.* 154–155 (2000) 659–663, [https://doi.org/10.1016/S0169-4332\(99\)00481-X](https://doi.org/10.1016/S0169-4332(99)00481-X).
- [13] S.I. Anisimov, B.L. Kapeliovich, Electron emission from metal surfaces exposed to ultrashort laser pulses, *Zh. Eksp. Teor. Fiz.* 66 (2) (1974) 375–377.
- [14] K. Eidmann, J. Meyer-ter-Vehn, T. Schlegel, S. Hüller, Hydrodynamic simulation of subpicosecond laser interaction with solid-density matter, *Phys. Rev. E* 62 (1) (2000) 1202.
- [15] N.N. Nedialkov, S.E. Imamova, P.A. Atanasov, P. Berger, F. Dausinger, Mechanism of ultrashort laser ablation of metals: molecular dynamics simulation, *Appl. Surf. Sci.* 247 (1–4) (2005) 243–248.
- [16] S. Song, et al., A critical review on the simulation of ultra-short pulse laser-metal interactions based on a two-temperature model (TTM), *Opt. Laser Technol.* 159 (2023) 109001.
- [17] G. Lin, P. Ji, M. Wang, Y. Meng, Numerical insight into heat transfer in surface melting and ablation subject to femtosecond laser processing aluminum, *Int. Commun. Heat Mass Transfer* 142 (2023) 106649.
- [18] J. Zhang, Y. Chen, M. Hu, X. Chen, An improved three-dimensional two-temperature model for multi-pulse femtosecond laser ablation of aluminum, *J. Appl. Phys.* 117 (6) (2015) 063104.
- [19] L. Peng, et al., Numerical simulation and investigation of ultra-short pulse laser ablation on Ti6Al4V and stainless steel, *AIP Adv.* 13 (6) (2023) pp.
- [20] X. Wang, Y. Huang, C. Li, B. Xu, Numerical simulation and experimental study on picosecond laser ablation of stainless steel, *Opt. Laser Technol.* 127 (2020) 106150, <https://doi.org/10.1016/j.optlastec.2020.106150>.

- [21] P. Lickschat, D. Metzner, S. Weißmantel, Fundamental investigations of ultrashort pulsed laser ablation on stainless steel and cemented tungsten carbide, *Int. J. Adv. Manuf. Technol.* 109 (2020) 1167–1175.
- [22] L. Omeñaca, M. Gomez-Aranzadi, I. Ayerdi, E. Castaño, Numerical simulation and experimental validation of ultrafast laser ablation on aluminum, *Opt. Laser Technol.* 170 (2024) 110283, <https://doi.org/10.1016/j.optlastec.2023.110283>.
- [23] E. Bévilon, J.-P. Colombier, B. Dutta, R. Stoian, Ab initio nonequilibrium thermodynamic and transport properties of ultrafast laser irradiated 316L stainless steel, *J. Phys. Chem. C* 119 (21) (2015) 11438–11446.
- [24] D. Metzner, M. Olbrich, P. Lickschat, A. Horn, S. Weißmantel, Experimental and theoretical determination of the effective penetration depth of ultrafast laser radiation in stainless steel, *Lasers Manuf. Mater. Process.* 7 (2020) 478–495.
- [25] J. Sotrop, M. Domke, A. Kersch, H.P. Huber, Simulation of the melting volume in thin molybdenum films as a function of the laser pulse duration, *Phys. Proc.* 41 (2013) 520–523.
- [26] P.G. Klemens, R.K. Williams, Thermal conductivity of metals and alloys, *Int. Metals Rev.* 31 (1) (1986) 197–215.
- [27] C.S. Kim, Thermophysical properties of stainless steels. Argonne National Lab., Ill (USA), 1975.
- [28] C.A.J. Fletcher, Computational Techniques for Fluid Dynamics: Specific Techniques for Different Flow Categories, Springer Science & Business Media, 2012.
- [29] F. Di Niso, C. Gaudiuso, T. Sibillano, F.P. Mezzapesa, A. Ancona, P.M. Lugarà, Role of heat accumulation on the incubation effect in multi-shot laser ablation of stainless steel at high repetition rates, *Opt. Exp.* 22 (10) (2014) 12200–12210.
- [30] J. Bykskov-Nielsen, J.-M. Savolainen, M.S. Christensen, P. Balling, Ultra-short pulse laser ablation of metals: threshold fluence, incubation coefficient and ablation rates, *Appl. Phys. A* 101 (2010) 97–101.
- [31] P. Wang, Q. Peng, Unveiling of incubation and absorption-enhanced effects occurring during multi-shot femtosecond laser ablation of aluminum and steel surfaces, *Nanotechnology* (2023).
- [32] Y. Jee, M.F. Becker, R.M. Walser, Laser-induced damage on single-crystal metal surfaces, *JOSA B* 5 (3) (1988) 648–659.
- [33] X. Zhao, Y.C. Shin, Femtosecond laser ablation of aluminum in vacuum and air at high laser intensity, *Appl. Surf. Sci.* 283 (2013) 94–99.
- [34] D. Haasler, T. Schneider, R. Poprawe, Investigation of the ablation rate of stainless steel by means of few ultrashort laser pulses up to 150 J/cm², *J. Laser Micro Nanoeng.* 14 (3) (2019) 236–244.
- [35] P.T. Mannion, J. Magee, E. Coyne, G.M. O'Connor, T.J. Glynn, The effect of damage accumulation behaviour on ablation thresholds and damage morphology in ultrafast laser micro-machining of common metals in air, *Appl. Surf. Sci.* 233 (1) (2004) 275–287, <https://doi.org/10.1016/j.apsusc.2004.03.229>.
- [36] M.V. Shugaev, et al., Laser-induced thermal processes: heat transfer, generation of stresses, melting and solidification, vaporization, and phase explosion, in: *Handbook of Laser Micro-and Nano-Engineering*, Springer, 2021, pp. 83–163.
- [37] C. Wu, L.V. Zhigilei, Microscopic mechanisms of laser spallation and ablation of metal targets from large-scale molecular dynamics simulations, *Appl. Phys. A* 114 (1) (2014) 11–32.
- [38] M.E. Shaheen, J.E. Gagnon, B.J. Fryer, Femtosecond laser ablation behavior of gold, crystalline silicon, and fused silica: a comparative study, *Laser Phys.* 24 (10) (2014) 106102.
- [39] J. Hermann, S. Noël, T.E. Itina, E. Axente, M.E. Povarnitsyn, Correlation between ablation efficiency and nanoparticle generation during the short-pulse laser ablation of metals, *Laser Phys.* 18 (2008) 374–379.
- [40] N. Hodgson, H. Allegre, A. Caprara, A. Starodoumov, S. Bettencourt, Efficiency of ultrafast laser ablation in burst mode as a function of intra-burst repetition rate and pulse fluence, in: *Frontiers in Ultrafast Optics: Biomedical, Scientific, and Industrial Applications XXI* SPIE, 2021, p. 116760G.
- [41] R. De Palo, A. Volpe, C. Gaudiuso, P. Patimisco, V. Spagnolo, A. Ancona, Threshold fluence and incubation during multi-pulse ultrafast laser ablation of quartz, *Opt. Exp.* 30 (25) (2022) 44908–44917.
- [42] J.-M. Liu, Simple technique for measurements of pulsed Gaussian-beam spot sizes, *Opt. Lett.* 7 (5) (1982) 196–198.
- [43] G. Raciucaitis, M. Brikas, P. Gecys, M. Gedvilas, Accumulation effects in laser ablation of metals with high-repetition-rate lasers, in: *High-Power Laser Ablation VII*, Spie, 2008, pp. 725–735.
- [44] A. Orlandini, S. Baraldo, M. Porta, A. Valente, Ablation threshold estimation for femtosecond pulsed laser machining of AISI 316L, *Proc. CIRP* 107 (2022) 617–622.
- [45] T. Zhou, et al., Experimental and numerical study of multi-pulse picosecond laser ablation on 316 L stainless steel, *Opt. Exp.* 31 (23) (2023) 38715–38727.
- [46] M.E. Shaheen, J.E. Gagnon, B.J. Fryer, Laser ablation of iron: a comparison between femtosecond and picosecond laser pulses, *J. Appl. Phys.* 114 (8) (2013) 083110.
- [47] M. Saghebfar, M.K. Tehrani, S.M.R. Darbani, A.E. Majd, Femtosecond pulse laser ablation of chromium: experimental results and two-temperature model simulations, *Appl. Phys. A* 123 (2017) 1–9.
- [48] P.B. Johnson, R.W. Christy, Optical constants of transition metals: Ti, v, cr, mn, fe, co, ni, and pd, *Phys. Rev. B* 9 (12) (1974) 5056.
- [49] L. Zhang, X.W. Cao, S.G. Li, R.Y. Xiang, H.C. Sun, Investigation of femtosecond laser ablation threshold for nickel template, *Appl. Mech. Mater.* 633 (2014) 665–670.
- [50] S. Nolte, et al., Ablation of metals by ultrashort laser pulses, *JOSA B* 14 (10) (1997) 2716–2722.
- [51] J. Winter, M. Spellauge, J. Hermann, C. Eulenkamp, H.P. Huber, M. Schmidt, Ultrashort single-pulse laser ablation of stainless steel, aluminium, copper and its dependence on the pulse duration, *Opt. Exp.* 29 (10) (2021) 14561–14581.
- [52] T. Pflug, et al., Fluence-dependent transient reflectance of stainless steel investigated by ultrafast imaging pump-probe reflectometry, *J. Phys. Chem. C* 125 (31) (2021) 17363–17371.